Carbon 179 (2021) 337–347

Contents lists available at ScienceDirect

Carbon

journal homepage: www.elsevier.com/locate/carbon

High performance carbonized corncob-based 3D solar vapor steam generator enhanced by environmental energy

Yang Sun [a], Zongbin Zhao [a, *], Guanyu Zhao [a], Luxiang Wang [b], Dianzeng Jia [b], Yongzhen Yang [c], Xuguang Liu [c], Xuzhen Wang [a], Jieshan Qiu [a, d, **]

[a] State Key Laboratory of Fine Chemicals, Liaoning Key Laboratory for Energy Materials and Chemical Engineering, School of Chemical Engineering, Dalian University of Technology, Dalian, 116024, China
[b] Key Laboratory of Energy Materials Chemistry, Ministry of Education, Key Laboratory of Advanced Functional Materials, Autonomous Region, Institute of Applied Chemistry, Xinjiang University, Urumqi, 830046, China
[c] Key Lab of Interface Science and Engineering in Advanced Materials, Ministry of Education, Taiyuan University of Technology, Taiyuan, 030024, China
[d] School of Chemical Engineering, Beijing University of Chemical Technology, Beijing, 100029, China

ARTICLE INFO

Article history:
Received 12 January 2021
Received in revised form
2 April 2021
Accepted 9 April 2021
Available online 16 April 2021

Keywords:
Biomass
C-corncob
Interfacial solar steam generation
Salt deposition

ABSTRACT

Biomass-based materials usually evolve well-developed and unique structures for the transportation of water and nutrition to their pivotal organs. These natural intricate designs allow fascinating properties when harnessed in specific real-world application. Herein, we demonstrate that 3D carbonized corncob (C-corncob) harmoniously coordinates light absorption, water supply, vapor escape, and efficiently utilizes the environmental energy to enhance the performance of the steam generation device due to its multilevel inside and side surface structures. The interfacial solar steam generation based on C-corncob achieves as high as 4.16 kg m^{-2} h^{-1} evaporation rate under 1.0 sun illumination and readily overcomes the salt deposition problem. These findings not only demonstrate the competence of the recrement corncob as the lost cost material for interfacial solar steam generation, but also provide inspiration for the creation of solar steam generation devices with the new concept.

1. Introduction

The contradiction between supply and demand of freshwater is always the foremost challenge all over the world, especially in some drought regions, which has seriously hampered industrial and agricultural production and development [1]. As suggested by the World Health Organization, nearly half of the population will possibly suffer from the freshwater resource scarcity in the near future [2,3]. Myriad efforts have been taken in the preparation of freshwater to alleviate the negative effect of water deficit, including the multi-stage flash (MSF) [4], multi-effect evaporation (MED) [5], reverse osmosis (RO) [6], and solar desalination [7,8]. Among all available technique to seawater desalination, the conception of interfacial solar-driven steam generation (ISSG) has been proposed as a low-costing, clean, and sustainable promising technology to perfectly solve the issue of freshwater resource scarcity due to its capability of localizing solar energy at water/air interface and minimizing heat loss [9–11]. It is generally considered that the photothermal conversion materials (PCMs) of ISSG play a critical role in the interfacial solar vapor process [12–14]. Enormous PCMs with artificial and natural structures have been fabricated and investigated to enhance the photothermal conversion efficiency [15]. Over the early years, a variety of artificial structures have been designed to improve the solar absorption, minimize the heat loss and enhance water supply, such as zero-dimensional structure plasmonic-based noble metal nanoparticles [16–18], one-dimensional CNTs [19–21], two-dimensional graphene [22–24], and three-dimensional structure based on the gel and sponge with the stable performance of thermal insulation [25–31]. However, the poor extensibility and higher cost of artificial structures severely restricted the further development of ISSG.

Whereas, recently the main emphasis of research has shifted from the high cost and formulation difficulty of artificial structure systems to the aplenty natural structure to reduce cost and achieve

* Corresponding author.
** Corresponding author. State Key Laboratory of Fine Chemicals, Liaoning Key Laboratory for Energy Materials and Chemical Engineering, School of Chemical Engineering, Dalian University of Technology, Dalian, 116024, China.
E-mail addresses: zbzhao@dlut.edu.cn (Z. Zhao), jqiu@dlut.edu.cn (J. Qiu).

https://doi.org/10.1016/j.carbon.2021.04.037
0008-6223/

scalable production. Compared with artificial structures, natural structures possess internal well-defined channels, excellent thermal insulation performance, low-costing, and environmental friendliness. Massive natural structures based on the biomass materials, such as woods, straw, food waste, and biomass-derived aerogel, have been reported as new candidates for ISSG via various carbonization treatments [32–35]. More specifically, Zhu et al. demonstrated hierarchical porous carbonized mushrooms with a high evaporation rate under one solar irradiation [36]. Hu et al. achieve a high evaporation rate of 1.35 kg m^{-2} h^{-1} via 85% solar energy under one solar irradiation by using scalable surface carbonized woods [37]. Xu et al. developed four types of solar absorbers with different shapes and nanostructures on the basis of recycled biomass E. prolifera after high-temperature pyrogenation [38]. Tan et al. have developed a simple and cost-effective carbonization process mimicking outdoor barbeque cooking for the preparation of carbon materials from food wastes, including rice, potato, pasta, banana peel, lotus root, and moldy bread et al. [39,40]. However, the limited theoretical evaporation rate (only 1.47 kg m^{-2} h^{-1} under 100 mW cm^{-2} of solar illumination assuming 100% solar-to-vapor energy conversion efficiency), the discontinuity of sunlight during a day and the inevitable salt deposition remains great challenges in satisfying further development of ISSG on the basis of natural biomass-materials [39–41].

Corn is widely cultivated in tropical and temperate regions of the world. Typical corn reaches maturity within months and provides people and animals with abundant foods, therefore, the corncob is one of the most renewable resources after corn kernels threshing [42,43]. Natural corncob (N-corncob) plays an important role in the growth process of corn, which transports a large amount of water and nutrient for transpiration and growth of corn kernels depending on its unique and delicate network structure. The mechanism of water transport in N-corncob is the synergistic effect of transportation and storage, which ensure the healthy development of corn grains [44–46]. In view of this, we have formulated a new value strategy for the higher value application of N-corncob through low-temperature carbonization. The ISSG on the basis of corncob has been carried out for desalination and sewage treatment through the utilization of N-corncob. Moreover, compared with other biomass carbonization processes, the lower carbonization temperature makes it possible to keep the original structure, better mechanical properties and excellent hydrophilic properties of the corncob.

Herein, inspired by N-corncob, we demonstrate that carbonized corncob (C-corncob) can act as an ideal ISSG device due to its unique structure. It is informed that C-corncob possesses a multi-hierarchical porous structure and a high capability of utilizing energy input from the environment. The solar steam generator based on C-corncob achieves a water evaporation rate as high as 4.16 kg m^{-2} h^{-1} under one solar irradiation, as well as rapid water evaporation without solar energy input. It is also worth noting that the solar vapor generator exhibits superior stability without any evaporation rate degradation after 26 days cycles and excellent performance for salt resistance. As the byproduct of corn production, corncob has the potentials for the creation of a new solar-vapor steam generator due to its unique structure, large abundant resource, and green preparation process.

2. Experimental section

2.1. Materials preparation

Fresh corns used in experiments were bought from the vegetable market (Dalian, Liaoning Province, China). After threshing treatment (Fig. S1), the obtained corncob was immersed into 1 M NaOH for 60 min. Then the corncob was washed to pH of 7 by deionized water and dried at 80 °C for 12 h. The dried corncob was subjected to pyrolysis in N_2 atmosphere. Firstly, the dried corncobs were heated to 300 °C and maintained for 30 min, and then further to 450 °C for 60 min. After naturally cooling to room temperature, the carbonized corncob (C-corncob) was washed with water and alcohol for several times to remove impurity, finally drying in 80 °C for 12 h. The aspect ratio of C-corncob used in the experiment was about 6.1 (Height: 12.5 cm, Diameter: 2.5 cm). C-corncobs were also prepared at different temperatures in addition to 450 °C, without any special illustration, the C-corncob refers to the material prepared at 450 °C.

2.2. Characterization

The microscopic morphology of natural and carbonized corncobs was characterized by a field emission scanning electronic microscope (FESEM, FEI Company, NOVA Nano SEM 450). A Lambda 950 Vis/NIR Spectrophotometer (PerkinElmer) attached with an integrating sphere was used for the absorbance of the samples. Fourier transform infrared spectra (FTIR) were obtained on a VERTEX70 spectrometer. X-ray photoelectron spectroscopy (XPS) experiments were carried out on a K-Alpha spectrometer (Thermo Fisher Scientific Inc., Switzerland) equipped with a monochromatic Al Kα source operated at 150 W. All spectra were calibrated based on the C 1s binding energy at 284.6 eV. Ions concentrations were measured by inductively coupled plasma optical emission spectrometer (EP Optimal 8000).

2.3. Solar vapor generation

A solar simulator (CEL-S500) equipped with an AM1.5 filter for the standard air mass 1.5-G spectrum was used as the illumination source. A white heat shield is place on directly above the sample to ensure that the size of the light spot is equal to that of the absorber, which avoid the heat to the environment or container. Once the light was projected on the surface of the sample, the weight change of the evaporation system was recorded by a 4 decimal electronic precision analytical balance (CP214) without wind shield, which was connected to a desktop computer by a serial communication module (RS232). The illumination intensity was calibrated with a light intensity meter (air cool thermopile sensor with a 10 mm diameter detector, CEL-NP2000). An infrared camera (FOTRIC 237) was used to capture the temperature files and was calibrated using thermocouples. The measurement uncertainty of the calibrated IR camera was about 1.0 °C.

2.4. Test of thermal conductivity

The Flash Method technique was used for the determination of thermal diffusivity on a Netzsch LFA 447 Nanoflash. The thermal conductivity of the C-corncob can be calculated with the formula, which is showed below.

$$\alpha = \lambda / c\rho$$

where α is thermal diffusion coefficient (0.369 mm2 s-1), λ is heat conductivity, ρ is density of the material and is specific heat (0.3 J g-1 °C −1).

3. Result and discussion

Fig. 1 presents the design concept of a solar-vapor steam generation device based on C-corncob. N-corncob is prepared after the removal of kernels from corn ear and transformed into C-corncob

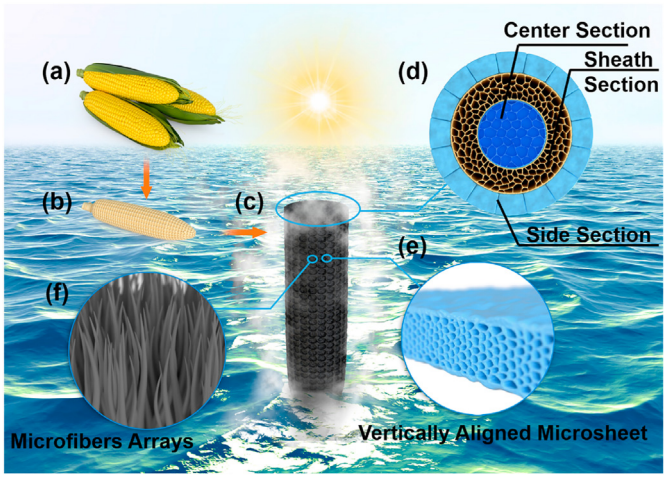

Fig. 1. Schematic of C-corncob based solar vapor steam generator. (a) Corn ears. (b) N-corncob. (c) C-corncob based solar vapor generation device. (d) cross-section of C-corncob. (e) aligned porous sheet on side surface of C-corncob. (f) carbon microfiber arrays on the side surface of C-corncob. (A colour version of this figure can be viewed online.)

by carbonization at low temperature (as shown in Fig. 1 a and b). As presented in Fig. 1c, the C-corncob is fixed onto the surface of water with most of its body (90%) exposed in the air. As revealed in Fig. 1d, the cross-section of the C-corncob can be divided into three parts, including the central section, the sheath section and the side section. The side surface of the C-corncob is decorated with aligned porous sheets (Fig. 1e) and carbon microfiber arrays (Fig. 1f).

As well known, grain arrays of corn orderly grow on the surface of N-corncob along its axis. After the removal of corn grains from the corn ear, the exposed side surface of the N-corncob is decorated with well-defined arrays of pits inherited from original grain arrays and sheet-like materials (Fig. 2e and Fig. S1). As shown in Fig. 2a, the cross-section of the N-corncob exhibits a soft white sponge structure in its center, which is embraced by a hard shell. Meanwhile, the hard shell is grown outmost with the sheet-like materials. After low-temperature carbonization, N-corncob is transformed into black C-corncob (as shown in Fig. S2) with nearly 20% volume shrinkage. Correspondingly, the resultant C-corncob is consisted of three parts from inside to outside in the cross-section, including the central section, the sheath section concentrically surrounded the center and the rough side surface grown with perpendicular sheet-like materials. The center section of the C-corncob exhibits a sponge-like structure with the closed-packed interconnected pores ranging from 70 to 120 μm (as shown in Fig. 2b), which is conducive to water storage and solar light absorption for solar steam formation. Fig. 2c shows the microstructures of the sheath, which consists of well-defined microchannels along the axis of C-corncob, similar to the wood structures reported by Hu's group previously [35]. It is reasonable to believe that these microchannels in the pristine N-corncob are responsible for the transportation of water and nutrients during the growth of corn. Therefore, these microchannels in the C-corncob will guarantee adequate water transportation and supply during the solar steam generation process and also benefit solar energy capturer. Fig. 2d further presents the detailed structures of the microchannels, there exist abundant micropores with a diameter of about 5 μm in their interior wall, forming a three-dimensional interconnected network structure within the sheath.

As presented in Fig. 2e, sheet-like arrays are grown on the side surface of the N-corncob perpendicular to its axis. These arteries and vein-like structures constitute a three-dimensional network within the sheet (the schematic as shown in Fig. S3c), guaranteeing rapid and directional water transmission from the interior to the side surface of C-corncob. Based on the pore diameter measurement (Fig. S4), these microchannels and branch connection channels are dominated with 8 μm and 1.5 μm diameter pores, respectively. Interestingly, there are abundant carbon microfibers grown on the side surface of C-corncob in addition to the sheet-like structure (Fig. 2h and Fig. S5). The length of microfibers is about 400 μm and the diameter is nearly 12 μm (Fig. 2h). It should be noted that the microfibers possess cone-like end, hollow interior structure (as shown in the insert of Fig. 2h), and micro-grooves

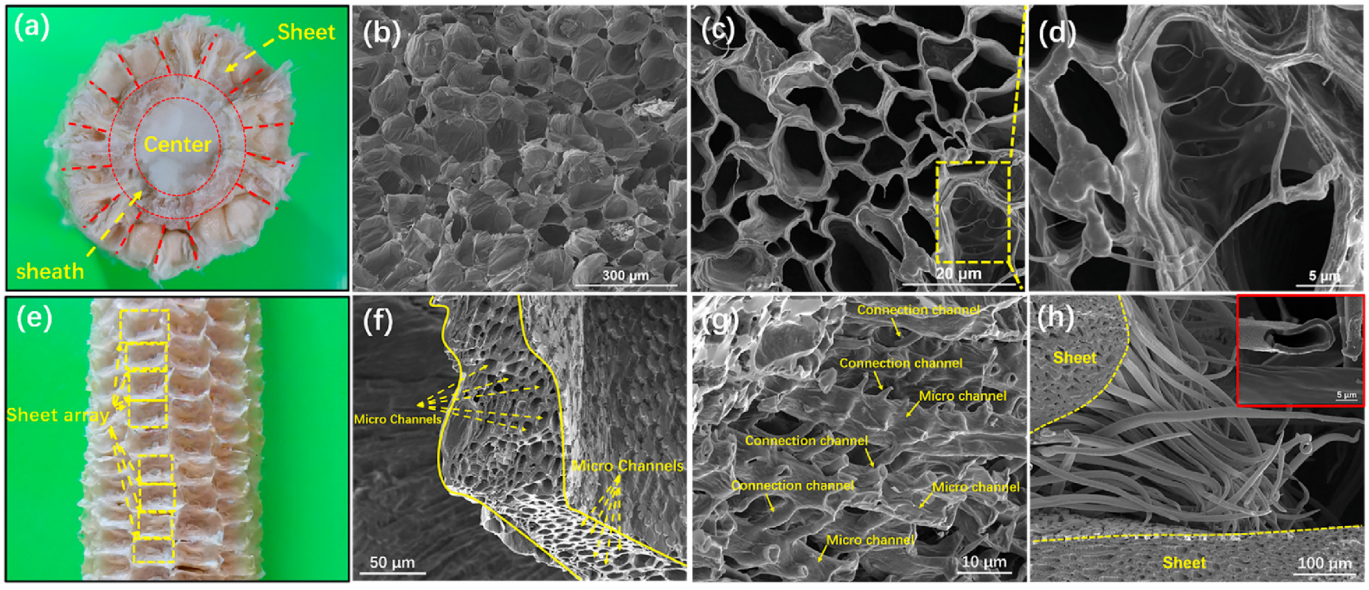

Fig. 2. Structures of the C-corncob. (a) Digital photo of N-corncob cross-section. (b–d) and (f–h) FESEM images of C-corncob structures: (b) sponge-like porous center; (c) sheath structure with microchannels; (d) interlinking junction of microchannels in sheath; (e) Digital photo of N-corncob side view; (f) a porous sheet grown on side surface; (g) the inner three-dimensional channel structure in a split sheet; (h) microfiber arrays grown on the side surface (Insert: showing the microfiber with hollow structure). (A colour version of this figure can be viewed online.)

embedded surface. In this sense, these carbon microfibers in the C-corncob might be beneficial to the escape of vapor during solar evaporation. In summary, the hierarchical and ingenious structures of C-corncob are consisted of sponge-like center, microchannel containing sheath, porous sheet-like structure, and hollow microfibers, which are precisely integrated together to compose a well-developed network, enabling smooth water transport and vapor escape during the process of solar steam evaporation.

The surface compositions and functional groups of the corncob-based materials are analyzed by the X-ray photoelectron spectroscopy (XPS) and Fourier transform infrared (FTIR) spectroscopy. The XPS survey spectrums of the corncob-based materials (Fig. 3a) present three main elements including carbon element (284.6 eV), oxygen element (532.2 eV) and nitrogen element (399.4 eV) in both N-corncob and C-corncob [47]. After carbonization, the intensity of C1s peak significantly increases, accompanied by the peak intensity reduction of both O1s and N1s. The C 1s XPS spectrums of N-corncob and C-corncob all show three peaks entered at 284.6, 285.6 and 289.1 eV (as shown in Fig. 3b and c), corresponding to the C–C, C–OH/C–N and C=O bonds, respectively [48]. Obviously, the intensity of C=O peak significantly increases in C-corncob compared with that in N-corncob. The FTIR spectrum (as shown in Fig. 3d) of the obtained C-corncob further confirms the existence of the C–N/N–H functional groups with the corresponding peak of 1041 cm^{-1} and 3415 cm^{-1}, respectively. Meanwhile, the strong peaks at 1124 cm^{-1} and 1605 cm^{-1}, corresponding to the C–OH stretching peak and C=O stretching peak, respectively, are observed in both N-corncob and C-corncob [49]. The surface of the C-corncob is highly hydrophilic due to the functional groups and elementary composition, which is beneficial for efficient water absorption and transportation. In addition, as shown in Fig. S6, we present the wetting property of C-corncob in different sections, including the centric section, the sheath section in the top side, and the side surface. The contact angle of the side surface in the C-corncob is about equal to 5°, indicating the superhydrophilicity of this section (Fig. S6a). We also observed the similar phenomenon in the sheath section consisting of many microchannels (Fig. S6b). Therefore, the superhydrophilicity of the sheath section and the side surface guarantees adequate water transportation and supply for the solar-vapor steam generation. However, the measured contact angle of the centric part with foam-like structure (Fig. S6c) was about 67°, suggesting that the center section possessed medium hydrophilicity. Considering the wettability and structure of the center part, the main function of the center section is supposed to as water reservoir and solar energy absorption rather than water transportation during solar steam generation.

Optical absorption is another critical feature impacting solar-vapor generation. The optical absorption properties of the corncob-based materials are evaluated by an ultraviolet–visible–near-infrared (UV–Vis–NIR) spectrophotometer. As presented in Fig. 3e, the C-corncob exhibits high (94–98%) light absorption over the whole wavelength range of 300–2500 nm while the pristine N-corncob shows much lower (about 15–20%) light absorption over the wavelength range of 500–1500 nm. Furthermore, we also compare the optical absorption ability of dry with that of wet C-corncob. It is obvious that both the dry and wet C-corncobs show a similar light absorption in the visible wavelength region, while the latter shows stronger light absorption in near-infrared wavelength region. As reported in the previous literature [50,51], the wavenumber dependence of the NIR optical absorption is determined by the difference between the relative refractive index of the material surface and the surrounding medium. Accordingly, the great refractive index difference between porous dry C-corncob and air leads to strong reflectivity, however, the light absorption in the NIR region of the wet C-corncob is enhanced by replacing air with the water thin layer in the pores due to the reduced difference of the relative refractive index between water film and materials surface. In addition, the sponge-like structures in the center of the C-corncob can act as traps for photon capture and thus benefits solar absorption.

As presented in Fig. S7, the density of dry C-corncob is only 188.7 kg m^{-3}, ~50% that of pristine corncob (350.2 kg m^{-3}), while the density of wet C-corncob in the solar evaporation is ~700 kg m^{-3}, suggesting the excellent water adsorption capability of this material. Although the thermal conductivity of C-corncob is higher than that of the N-corncob regardless in dry or wet state, the

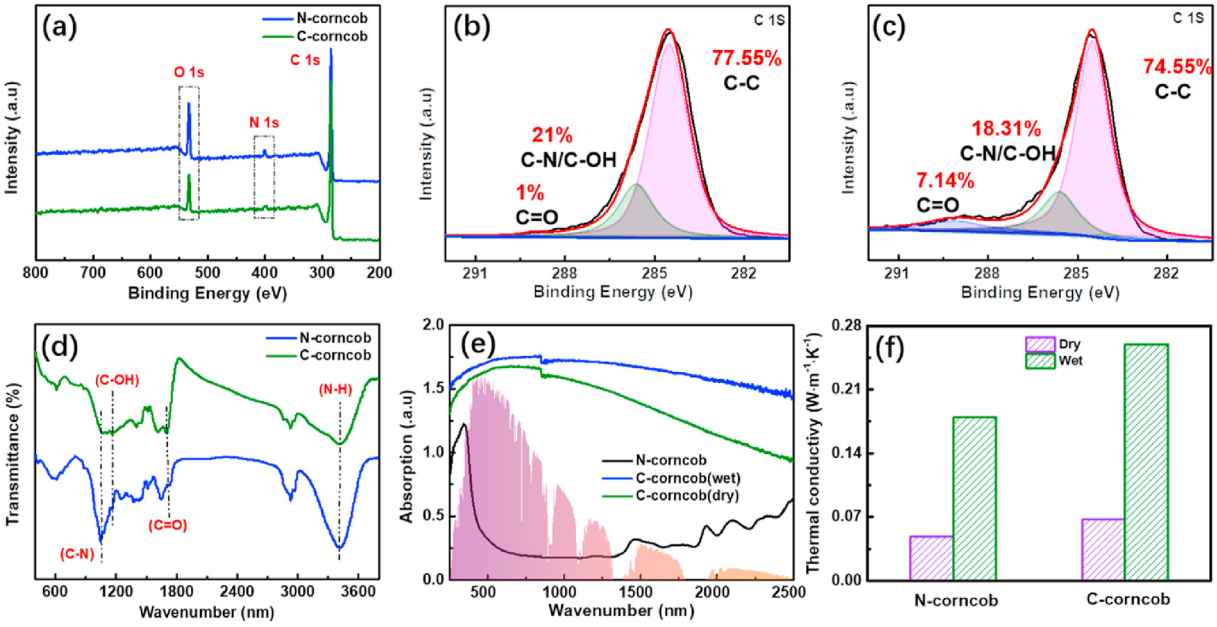

Fig. 3. Characterization of N-corncob and C-corncob. (a) XPS survey spectra. (b) XPS survey spectra of C 1s for N-corncob. (c) XPS survey spectra of C 1s for C-corncob. (d) FTIR spectra. (e) Light absorption spectra for N-corncob, C-corncob (dry) and C-corncob (wet) (f) Thermal conductivity of materials. (A colour version of this figure can be viewed online.)

wet C-corncob still shows a much lower thermal conductivity (0.27 W m^{-1} K^{-1}) than that of pure water (~0.6 W m^{-1} K^{-1}) [45] (Fig. 3e). This lower thermal conductivity of wet C-corncob benefits the heat localization during the solar evaporation and efficiently suppresses the heat dissipation to bulk water. The mechanical property of materials is critical for the long-term performance of solar evaporator, therefore, the mechanical properties of the C-corncob were evaluated, as shown in Fig. S8. The maximum load of N-corncob is up to nearly 2300 N, indicating the excellent mechanical property of the original material (Fig. S8a). Although the compressive property of C-corncob decreases after low-temperature carbonization, its maximum load is still as high as about 300 N (Fig. S8b). In addition, the C-corncob barely deforms under heavy pressure for 1 h (Fig. 1c), revealing the good stability of C-corncob (Fig. S8c). Compared with some other carbonized biomass materials (such as wood, mushroom and bamboo, Fig. S8 d-f), the compressive strength of the C-corncob is weaker than that of wood-derived carbon, similar to that of bamboo-derived carbon and much better than that of mushroom derived carbon. The good mechanical property of C-corncob guarantees continuous steam generation of device under harsh conditions.

Thermal management is of critical importance in improving the overall photothermal conversion efficiency in solar interfacial steam generation devices. The thermal properties of the C-corncob are evaluated with an Infrared camera. The overall temperature profile of the cross-section in dry C-corncob under one solar irradiance is shown in Fig. 4a. The temperature increases from the edge and reaches a maximum in the center, then decreases symmetrically in the opposite. It should be noted that the maximum temperature in the center of dry C-corncob is closed to 85 °C under one solar irradiation, which is higher than most photothermal conversion materials reported so far [52], indicating the excellent photothermal properties of the C-corncob. Furthermore, the side temperature profile along the longitudinal direction in dry C-corncob under one solar irradiance on top is also examined, as shown in Fig. 3b. The maximum temperature at the top is about 60 °C and decreases rapidly to about 26 °C within 2 cm in the longitudinal direction, indicating the poor thermal conduction along this direction and effective thermal confinement of N-corncob.

The temperature profiles over the top and along the side surface of the wet C-corncobs both in dark and under solar irradiation (one sun) are investigated and compared (as shown in Fig. 4c and d). In the case of dark (Fig. 4c), once the C-corncob was put in contact with water (25 °C), the temperature over the top and along the side surface reduces to 19 °C and 18 °C within 12.5 min, respectively. The temperature is decreasing results from the water evaporation on the surface of C-corncob owing to the intervention of environmental energy. The resultant temperature difference between the surface of C-corncob and environment would further enhance the input of environmental energy from both top and side surface. Once upon the introduction of one solar irradiation (on top), the temperature over the top surface increases to 37.8 °C within 7.5 min due to the impact of light irradiation, while the temperature of the side surface keeps invariably 18.5 °C (Fig. 3d), much lower than the environmental temperature (25 °C). This means the occurrence of water evaporation along the side surface of the C-corncobs by utilizing environmental energy. In other words, for the C-corncob under solar irradiation, water evaporation takes place both on the top surface driven by the light and on the side surface driven by the environmental energy, respectively.

The experimental results reveal that the optimum carbonization temperature for the preparation of C-corncob is about 450 °C based on water evaporation performance of the materials prepared at different carbonization temperatures under one sun irradiation (as presented in Fig. S9). C-corncob prepared from a lower temperature (350 °C) exhibit poor light absorption ability due to incomplete carbonization (Fig. S10), while higher temperature (550 °C) carbonization causes reduced hydrophilicity (Fig. S11). As a result, the materials from lower temperature and higher temperature carbonization show a slow evaporation rate (Fig. S9). Moreover, as shown in Fig. S12, according to the infrared digital photograph, water can be quickly pumped up to the top of the C-corncob within 5 min by capillary force with almost 90% length of the C-corncob exposed in the air. And the N-corncob can absorb three times weight of water compared with itself weight (as shown in Fig. S13). This phenomenon indicated that the capillarity effect in C-corncob could pump the water rapidly from bottom up to the evaporation area, which was crucial to the solar-vapor steam generation process. Furthermore, once the evaporation rate reaches stability, the mass of the wetted C-corncob keeps unchanged with time during evaporation under one solar irradiation, which indicates the adequate supply of water for evaporation (as shown in Fig. S14).

The evaporation rates under different solar illumination intensities are shown in Fig. 5a. The evaporation rate for the C-corncob under the illumination intensity of 20, 40, 80, 100, 140 mW cm^{-2} is 1.58, 2.24, 3.35, 4.16, 4.49 kg m^{-2} h^{-1}, respectively. It is worth mentioning that the ISSG based on C-corncob exhibits a high evaporate rate under low solar intensity, indicating the potential application in actual conditional environment. The enhanced factor is estimated through the following equation [53]:

$$\text{Enhanced factor} = v/ \qquad 1.47s$$

where v is the water evaporation rate under different solar irradiation, 1.47 is the theoretical evaporation rate under 100 mW cm^{-2} of solar illumination assuming 100% solar-to-vapor energy conversion efficiency, and s is the solar intensity. According to the above equation, as shown in Fig. 5b, the estimated enhanced factor under different illumination intensity of 20, 40, 80, 100, 140 mW cm^{-2} is 5.41, 3.87, 2.85, 2.74 and 2.31, respectively, indicating the significant contribution of environmental energy during C-corncob solar evaporation process. However, the enhanced factor decreases with the increase of solar intensity. The effect of C-corncob length exposed in the air on the evaporation rates under one solar illumination is investigated. Obviously, the evaporation rate decreases with the increase of length submerged in water. To further clarify the relative contribution from environmental energy input, the side surface evaporation is excluded by completely immersing C-corncob into water with only its top surface exposed in the air or fully sealing the side surface with adhesive tap during solar steam evaporation. As shown in Figs. S15 and S16, the corresponding evaporation rate for the immersed and sealed C-corncob under one solar irradiation is 1.98 and 1.93 kg m^{-2} h^{-1}, respectively. In other words, the evaporation rate from the top surface is much lower than that from the simultaneous top and side surface evaporation. Therefore, we demonstrate the great contribution from the environmental energy during solar-driven water evaporation over the C-corncob. However, it should be noted that the evaporation rate from top surface is still above the theoretical solar evaporation limit value. Differential scanning calorimetry experiments exhibit a reduced vaporization enthalpy (1774 J g^{-1}) over C-corncob compared with that of free evaporation water (2406 J g^{-1}), shown in Fig. S17 and Table S1. As reported by Yu et al. [27], when water molecules are confined to three-dimensional through hole, the water can escape from the samples surface in form of water cluster rather than single molecule. The water molecular cluster mediated evaporation results in significant reduction in water vaporization enthalpy (from 2406 to 1774 J g^{-1}). In addition, the Raman analysis of water (Fig. S18) and Li^{+} content

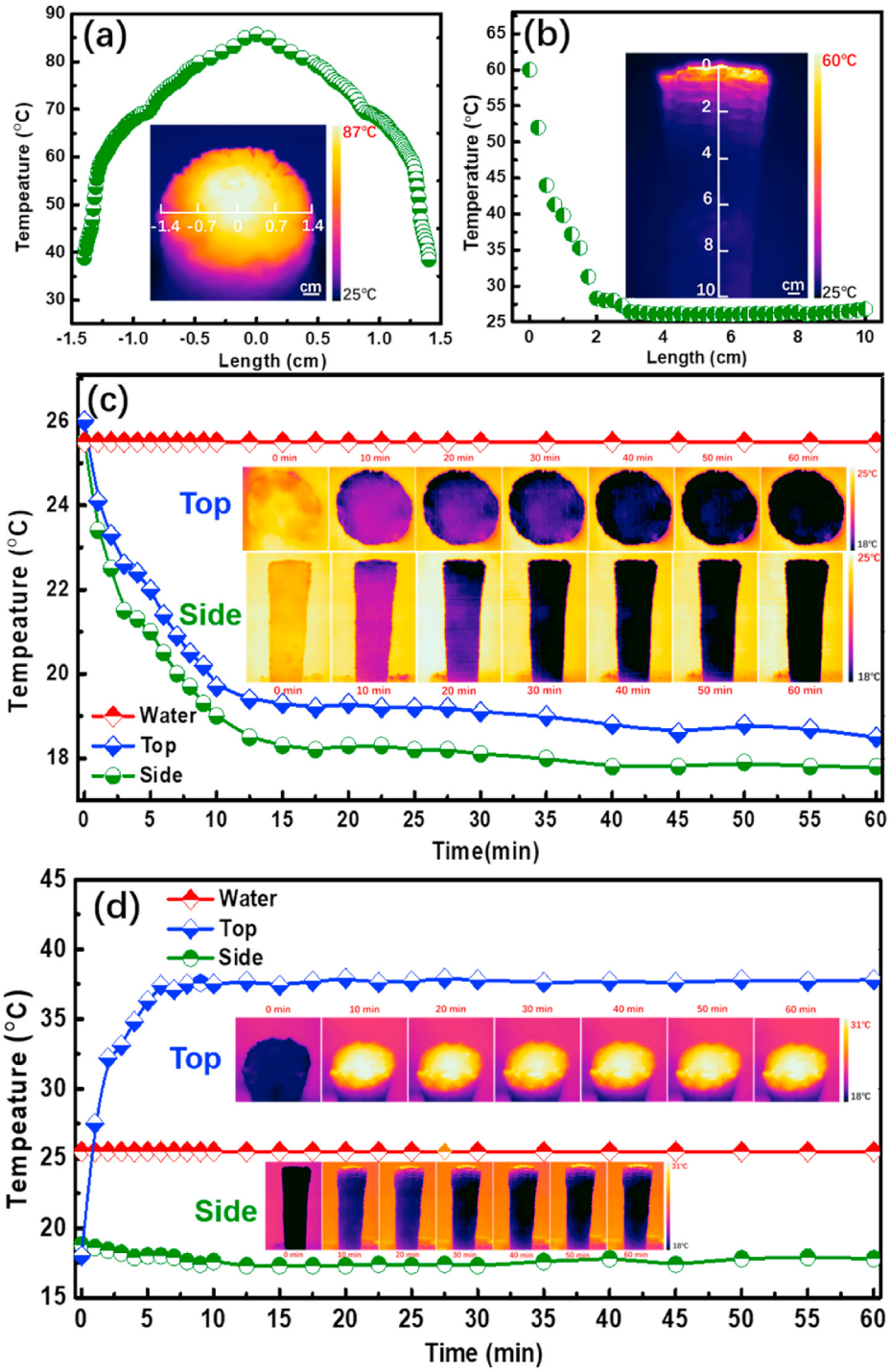

Fig. 4. Temperature profiles of C-corncob under different conditions. (a) top surface under one solar irradiation in dry state. Inset: IR image of top surface. (b) side surface temperature profiles under one solar irradiation on top surface in dry state. Inset: IR image of side surface. (c) top and side temperature change of C-corncob as the function of time during water evaporation under dark condition. Inset: IR images of top surface and side surface under dark. (d) top and side surface temperature change of C-corncob as a function of time during water evaporation under one solar irradiation. Inset: IR images of top surface and side surface. (A colour version of this figure can be viewed online.)

measurement in evaporation water from LiCl aqueous solution (Fig. S19) further confirm the water molecular cluster mediated evaporation. As summarized in Fig. 5c, the evaporation rate and efficiency of ISSG based on C-corncob have been compared with results recently reported. Obviously, the ISSG based on C-corncob achieved highest evaporation rate with high evaporation efficiency. Based on these above-mentioned factors, the excellent water evaporation performance of C-corncob can be attributed mainly to several factors, including the efficient solar thermal conversion, excellent restriction of thermal heat loss, rational water transportation pathway, energy gained from the environment and the reduced evaporation enthalpy of water. Most importantly, the results show the weaker the light intensity, the more the relative contribution from the environmental energy. Taking into

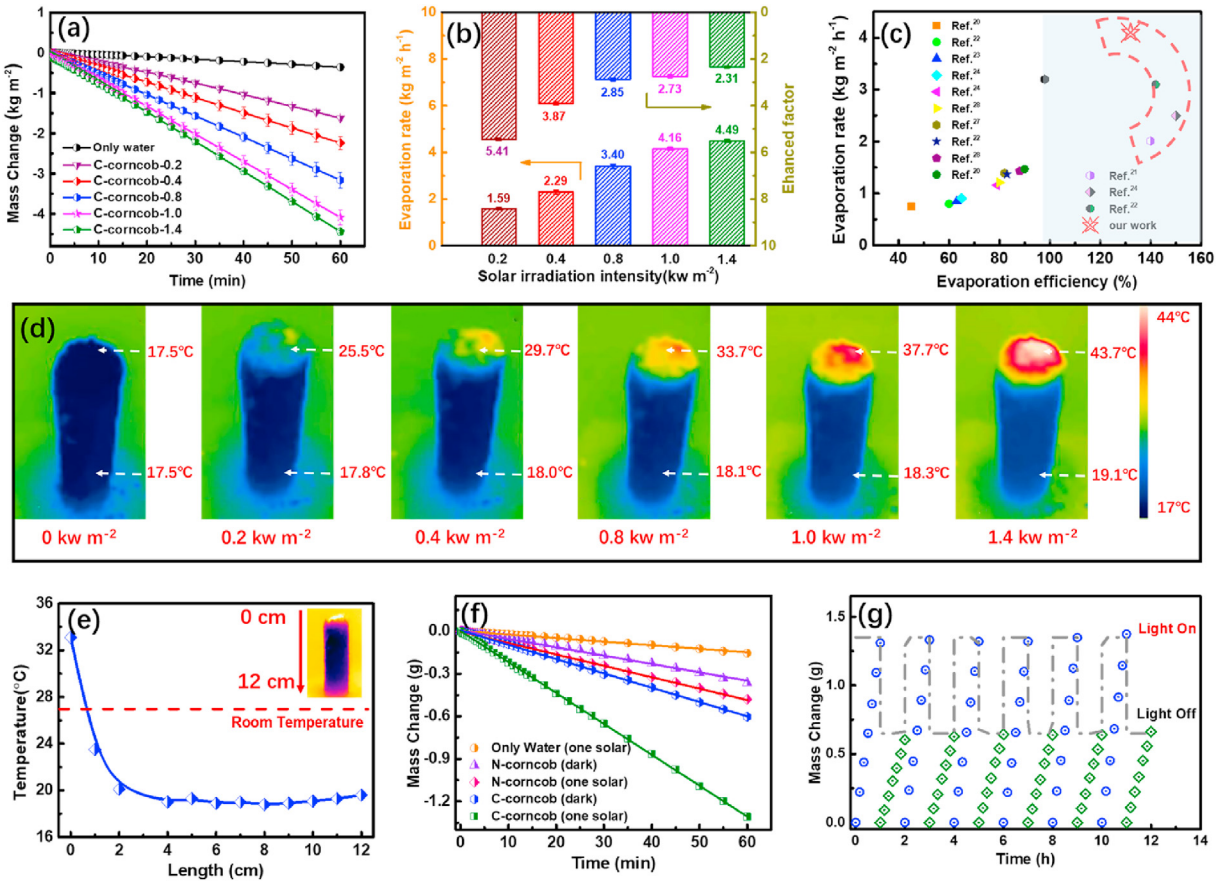

Fig. 5. Performance of corncob-based solar vapor steam generator. (a) Water mass changes as a function of time over C-corncob under different light intensities. (b) Evaporation rates over C-corncob under different light intensities and corresponding enhanced factors. (c) Comparison of evaporation efficiency and evaporation rate over C-corncob with previous reports under one solar irradiation. (d) Infrared images of the C-corncob under different light intensities (for 60 min). (e) Temperature profile of the side surface of the C-corncob under one solar illumination on top after water evaporation for 60 min. The top of the C-corncob is set as the zero point of the height. (f) The mass changes of water over C-corncob and N-corncob as the function of time under one solar illumination and in dark. (g) Water mass changes over C-corncob under one solar illumination and in dark alternately for 12 h. (A colour version of this figure can be viewed online.)

consideration of the general low light intensity in real weather, the C-corncob based vapor generator is conducive to practical application.

The effect of solar illumination density on the temperature of both the top surface and side surface of the C-corncob (Room temperature 25 °C) during steam generation was investigated (Fig. 5d). An infrared camera was used to measure the temperature profile of the top and the side surface of the vapor generator under different illumination intensity of 20, 40, 80, 100, 140 mW cm^{-2}. As shown in Fig. 5d, the corresponding average temperature of top (and side) surface was 25.5 °C (17.8 °C), 29.7 °C (18.0 °C), 33.7 °C (18.1 °C), 37.7 °C (18.1 °C) and 43.7 °C (19.1 °C), respectively. Evidently, the temperature of the top surface increases with the increase of light illumination intensity, while the temperature of the side surface almost keeps constant and much lower than the environmental temperature. The top surface of the C-corncob directly absorbs the light energy, which results in the increasing temperature. However, the water evaporation on the side surface leads to its temperature decreasing (Fig. 5e) and temperature gradient between the side surface of C-corncob and environment. As a result, the side surface inputs energy from the surroundings via thermal conduction, convection, and radiation, greatly enhancing the water evaporation.

The water evaporation rate comparison over C-corncob and N-corncob under one solar illumination and in dark were summarized in Fig. 5f. The C-corncob exhibits a much higher evaporation capacity than the N-corncob both under solar irradiation and in the dark. It is worth mentioning that the mass change of water over the C-corncob in dark is nearly 50% the value under one solar illumination. Furthermore, we alternately switched on and turned off the light source to simulate daytime and night, as shown in Fig. 5g, the generator maintained stable evaporation efficiency during the test time (12 h) even in the absence of light, which indicates that the C-corncob steam generator could overcome the limitation of sunshine duration by efficiently utilizing external energy. This feature is critical for real application as a full-time vapor generator. Furthermore, we also investigated the water evaporation performance of C-corncob at different ambient temperatures (as shown in Fig. S20). The surface temperature of C-corncob is always lower than the environmental temperature, indicating the side surface still could harvest energy from the environment even in harsh ambient temperatures. The mass change measurement under different environmental temperature (as shown in Fig. S21) exhibits that the evaporation amount of water over C-corncob was much higher than that of free water evaporation whether in dark or under one solar irradiation, indicating the high capability of C-corncob as an ideal candidate for the steam generator.

Desalination over the ISSG based on C-corncob is carried out with real seawater from the Bohai Gulf (average salinity, 35‰). As shown in Fig. 6a, the evaporation rate of the seawater is as high as 3.74 kg m^{-2} h^{-1}, which is nearly 13 times higher than the seawater free evaporation rate (0.27 kg m^{-2} h^{-1}) in the absence of C-corncob.

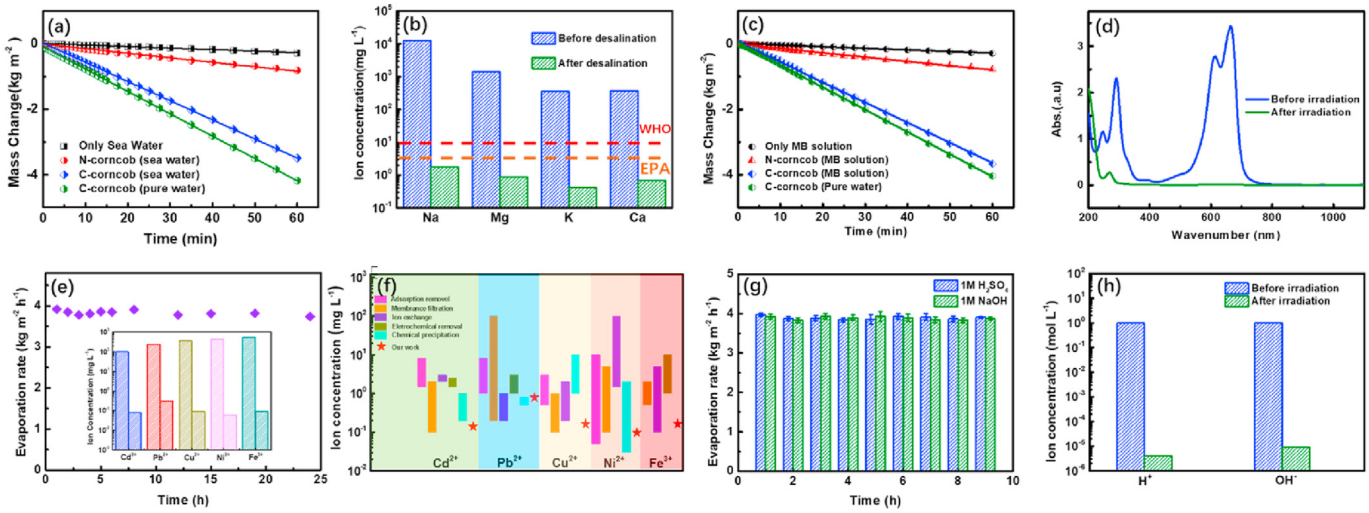

Fig. 6. Environmental energy-enhanced ISSG based on C-corncob for the purification of different types of water sources. (a) Evaporation rates of seawater over C-corncob and N-corncob under one solar illumination. (b) Measured concentrations of four primary ions in seawater before and after desalination. The dotted lines refer to the WHO and EPA standards for drinkable water. (c) Evaporation rates of dye solution (Methylene blue) over C-corncob and N-corncob under one solar illumination. (d) The UV–Vis–NIR spectra of Methylene blue solution before and after solar thermal purification. (e) The cycle stability of C-corncob in heavy metal solution (insert: measured concentrations of five primary ions in seawater before and after desalination). (f) Removing efficiency of C-corncob comparison with previous technologies in heavy metal solution. (g) The cycle stability of C-corncob in acid or alkali solution. (h) Measured concentrations of H^+ and OH^- in acid or alkali solution before and after irradiation. (A colour version of this figure can be viewed online.)

The evaporation rate of seawater over C-corncob is surely lower than that of the pure water (4.16 kg m^{-2} h^{-1}), which results from the increase of evaporation enthalpy of seawater caused by the existence of main ions. As shown in Fig. 6b, the concentrations of the main four ions (K^+, Na^+, Mg^{2+}, Ca^{2+}) in seawater and the formed water from evaporation are measured. After desalination, it is found that the concentrations of these ions are all significantly reduced (approximately four orders of magnitude), which are about two orders of magnitude lower than the drinking water standards formulated by the World Health Organization (WHO, 1‰) and the United States Environmental Protection Agency (EPA, 0.5‰). To further confirm the purity of water after desalination, we measure the Ohmic value of the water from a resistance test using a multimeter at constant distance between electrodes (as shown in Fig. S22), the resistance value of seawater, purified water and domestic water (from an urban water-supply company of Dalian, Liaoning, China) is 0.19 MΩ, 1.5 MΩ and 0.6 MΩ, respectively, suggesting effective purification of seawater via ISSG based on C-corncob. Salt durability of the C-corncob is indispensable for practical application. Our results show that (as shown in Fig. S23) the C-corncob solar vapor generator exhibits a stable evaporation rate under one solar illumination during 26 days for seawater desalination process. Importantly, the evaporation performance on the 1st day and 26th day keeps almost the same, indicating the high stability of C-corncob in the harsh seawater environment (as shown in Fig. S24).

In addition, solute accumulation at the heating interface severely impacts the performance and long-term stability of solar evaporation systems. Specifically, the precipitated salt from saturated water will accumulate at the evaporation interface and gradually block the water transport path, resulting in a significant decay of solar absorption and deterioration of steam generation. Generally, salt must be removed by backwashing or other post-treatment to regenerate the evaporator, thus reducing efficiency and increasing water production cost. However, the present ISSG based on C-corncob possesses excellent resistance to salt deposition due to its unique channel structure. In addition, as presented in Fig. S25, no salt deposition is observed at the surface of the evaporator after 20 h continuous under 1 sun irradiation or in dark, confirming the excellent self-regeneration properties of the three-dimensional C-corncob. FESEM further examination is used to evaluate salt deposition at the evaporator surface in the process of saltwater evaporation after 20 h continuous testing in 20 wt% NaCl solution under 1 sun irradiation (as shown in Fig. S26). Obviously, negligible salt deposition takes place at the sponge-like center section, while the microchannels in the side surface keep completely clean. The evaporation rate and stability in 20 wt% NaCl solution under one sun irradiation are shown in Fig. S27. The evaporation rate is about 2.7 kg m^{-2} h^{-1}, which is lower than that in pure water due to the higher surface tension in brine solution. However, the C-corncob presents excellent stability performance in 20 wt% NaCl solution under one sun irradiation for long time, indicating the potential application in harsh conditions with strong brine. Based on the results reported previously [54–58], it is speculated that spontaneous salt exchange between the channels leads to the salt dilution in the inner channels of the evaporation device. The good salt-resistance property of our C-corncob can be attributed to its interconnected hierarchical structures. For example, rapid transportation of the brine solution within the channels during the solar desalination process can be achieved. Specifically, the sheath section possesses abundant microchannels well-aligned along the corncob growth direction, which guarantees the sufficient brine solution upward. Meanwhile, the sheet-like arrays consist of abundant aligned microchannels and connect with the sheath section, which enables the formation of well-developed networks and allows lateral brine solution transportation, diffusion, and convection during desalination. As a result, the unique structure of the C-corncob makes it possible to avoid salt accumulation during solar desalination. In addition, the excellent hydrophilicity of C-corncob surface benefits the rapid replenishment of brine and avoids salt crystallization. In order to prove the salt-rejection ability of C-corncob, 0.6 g solid NaCl was put on the top surface and 1.0 g of solid NaCl on the side surface of the C-corncob, respectively (as shown in Fig. S28). It can be observed that most of the solid salt on both top surface and side surface disappears under one solar irradiation for 8 h. This experiment further demonstrates the C-corncob possesses excellent salt resistance ability.

To further expand the application of the ISSG based on C-corncob toward wastewater treatment, we evaluate the performance of C-corncob in the treatment of water containing Methylene blue (200 mg L^{-1}). In this case, the purification of Methylene blue solution can also be achieved by ISSG with an evaporation rate of 3.85 kg m^{-2} h^{-1} (Fig. 6c). As presented by an ultraviolet–visible–near-infrared (UV–Vis–NIR) spectrophotometer in Fig. 6d, the characteristic absorption peak (about 664 nm) of Methylene blue completely disappears in contrast to the raw Methylene blue. Clearly, the purified water becomes colorless after solar evaporation (as shown in Fig. S29). In addition, the recycle stability of C-corncob against heavy metal solution is investigated. As revealed in Fig. 6e, the C-corncob still maintains a stable evaporation rate after 25 h of continuous testing and the concentrations of the main five ions (Pb^{2+}, Cd^{2+}, Cu^{2+}, Ni^{2+}, Fe^{3+}) in heavy metal solution are all significantly reduced (as shown in insert of Fig. 6e). Compared with the main technique of treatment of water [59–62], as shown in Fig. 6f, the technology of ISSG based on C-corncob has a great advantage in removing efficiency of heavy metal ions. Furthermore, we also explore the cycle stability of C-corncob in acid or alkali solution. As presented in Fig. 6g, the C-corncob exhibits excellent evaporation stability in acid or alkali solution after 10 h irradiation under one solar intensity. As shown in Fig. 6 h, it is found that the concentrations of H^+ and OH^- are all significantly reduced six orders of magnitude after irradiation, indicating potential application of C-corncob in treating wastewater in harsh conditions. Therefore, the C-corncob based solar steam generator can be employed in the preparation of high-quality water regardless of seawater or wastewater.

Solar desalination based on C-corncob is performed outdoor to explore practicability. The digital photograph of the solar desalination device is illustrated in Fig. 7a. The prototype solar desalination device is divided into three parts, including water supply system, solar evaporation system and water reclamation system. The detailed structure of the solar evaporation system is presented in Fig. 7b. We adopt the structure of double-acrylic. The seawater comes through inlet into the upper container, then purified water condenses to the outer container by evaporation process based on C-corncobs and drains to water reclamation system. Herein, as presented in Fig. 7c, more than 26 C-corncobs with the height about 12 cm and diameter of about 2.5 cm are fixed to a foam thin disk over water in the inner of the device. The infrared images of those C-corncobs are presented in Fig. 7d, when the device is placed in opening outdoor without solar irradiation, the surface temperature (nearly 17 °C) of C-corncobs is still lower than the ambient temperature, indicating the abundant supply of seawater. Then an experiment was carried out from 6:00 to 18:00 in a typical day (as shown in Fig. 7e) with ample sunlight (the maximum solar intensity was nearly 0.85 kw m^{-2}). The mass of purified water is about 530 g from solar steam desalination (as shown in Fig. 7f), while almost 1500 g water removal from the system in opening environment (as shown in Fig. S30b), implying that much more purified water can be possibly obtained with proper condenser to remove vapor from the system timely. The total area of the solar evaporator consisted of 26 C-corncob samples is nearly to 430 cm^{-2} (the schematic of the total area is shown in Fig. S31). Thus, according to the mass of purified water (about 530 g) from the solar steam desalination device, the efficiency of clean water purification is about 12.32 kg m^{-2} in a natural day (24 h). Furthermore, as presented in Fig. S32, there exists much condensed water in the prototype solar desalination device at 3:00 compared with that at 21:00 according to the digital photo, indicating the evaporation process is ongoing for the duration of the night. Meanwhile, as revealed in Fig. 7f, the top surface temperature of C-Corncob samples increases to nearly 40 °C due to the closed system. To test the durability and stability of this prototype device, this experiment lasts for 20 natural days (as shown in Fig. S33). The relationships between the production of purified water and natural solar intensity, outdoor temperature are investigated. It could be observed that the mass of purified water increases with the increase of solar intensity and temperature. Moreover, even under the harsh weather with poor sunlight intensity (about 0.28 mW cm^{-2}) and low temperature (about 16 °C) (as revealed in Fig. S33a), we could still obtain about 100 ml purified water (as shown in Fig. S33b), which proves the practicability of the prototype water evaporation device.

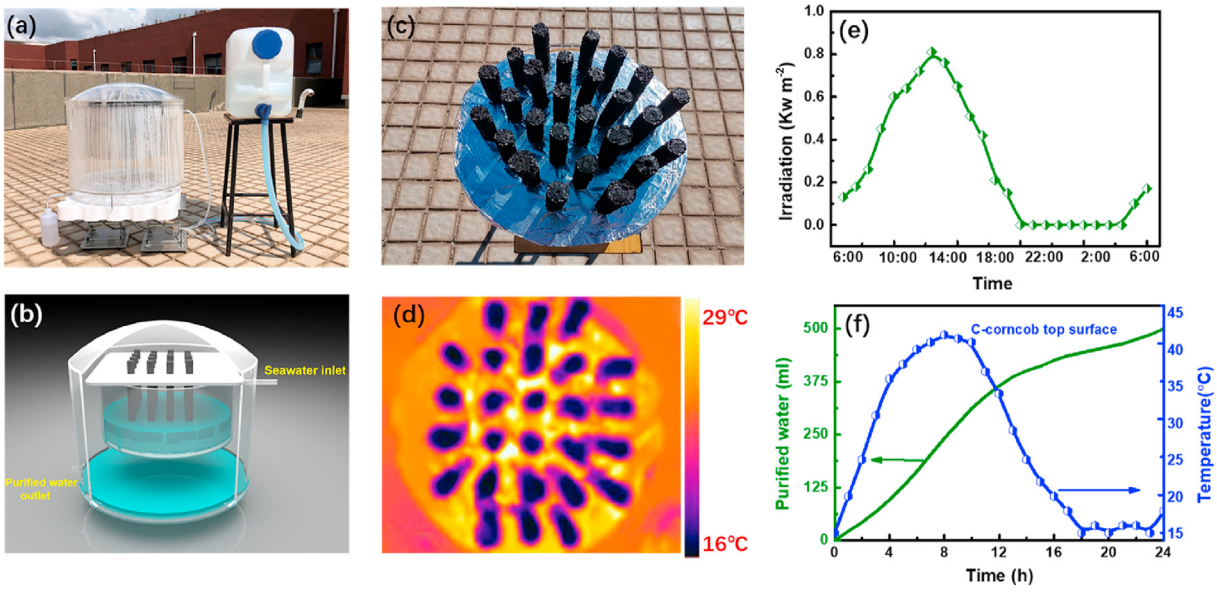

Fig. 7. Performance of C-corncob in outdoor desalination. (a) the digital photo of the prototype solar desalination device. (b) the schematic of prototype solar desalination device. (c) the digital photo of C-corncob forest. (d) Infrared images of the C-corncob forest. (e) the solar intensity changes under the sun from 6:00 a.m. to 6:00 (August 4th). (f) the temperature of C-corncob top surface, the mass of collected water changes under the sun from 6:00 to 6:00 in a natural day. (A colour version of this figure can be viewed online.)

4. Conclusions

In summary, we have demonstrated C-corncob as an ideal candidate for efficient solar steam interfacial generation because of its unique natural structures. The rational designed inside structures with abundant and 3D interconnected microchannels allow rapid water transportation within the whole C-corncob. The side surface of C-corncob possesses vertically grown porous sheets and carbon microfibers structures, which benefit the water evaporation by using environmental energy. The C-corncob based solar steam generator presents excellent light absorption, low thermal conductivity, rational water transport and vapor escape pathway. Ultrahigh water evaporation rate (4.16 kg m^{-2} h^{-1}) has been achieved over the C-corncob under one solar irradiation. Take into consideration the abundant resource of corncob, the simple preparation process of materials and the high performance of the reactors in the solar steam interfacial production, this corncob-based steam generator holds the promise of significantly expanding the application and reducing the cost of solar-powered water managing systems.

CRediT authorship contribution statement

Yang Sun: Materials preparation and characterization, Writing-Review. **Zongbin Zhao:** Guiding paper ideas, Writing-Reviewing. **Guanyu Zhao:** Data curation, Writing-Review. **Luxiang Wang:** Characterization of C-corncob. **Dianzeng Jia:** Materials characterization. **Yongzhen Yang:** Materials characterization. **Xuguang Liu:** Materials characterization. **Xuzhen Wang:** Materials characterization. **Jieshan Qiu:** Guiding paper ideas, Writing-Reviewing.

Declaration of competing interest

The authors declare that they have no known competing financial interests or personal relationships that could have appeared to influence the work reported in this paper.

Acknowledgement

The authors acknowledge the financial support of the National Natural Science Foundation of China (Grant No. U1703251, U1610255, 51672033).

Appendix A. Supplementary data

Supplementary data to this article can be found online at https://doi.org/10.1016/j.carbon.2021.04.037.

References

[1] M.M. Mekonnen, A.Y. Hoekstra, Four billion people facing severe water scarcity, Sci. Adv. 2 (2016), e1500323.
[2] J. Eliasson, The rising pressure of global water shortages, Nature 517 (2015) 6.
[3] T. Li, H. Liu, X. Zhao, G. Chen, J. Dai, G. Pastel, C. Jia, C. Chen, E. Hitz, D. Siddhartha, R. Yang, L. Hu, Scalable and highly efficient mesoporous wood-based solar steam generation device: localized heat, rapid water transport, Adv. Funct. Mater. 28 (2018) 1707134.
[4] T. Mezher, H. Fath, Z. Abbas, A. Khaled, Techno-economic assessment and environmental impacts of desalination technologies, Desalination 266 (2011) 263–273.
[5] V.G. Gude, Energy storage for desalination processes powered by renewable energy and waste heat sources, Appl. Energy 137 (2015) 877–898.
[6] S. Kim, K.H. Chu, Y.A.J. Al-Hamadani, C.M. Park, M. Jang, D.H. Kim, M. Yu, J. Heo, Y. Yoon, Removal of contaminants of emerging concern by membranes in water and wastewater: a review, Chem. Eng. J. 335 (2018) 896–914.
[7] C. Li, Y. Goswami, E. Stefanakos, Solar assisted sea water desalination: a review, Renew. Sustain. Energy Rev. 19 (2013) 136–163.
[8] H. Sharon, K.S. Reddy, A review of solar energy driven desalination technologies, Renew. Sustain. Energy Rev. 41 (2015) 1080–1118.
[9] H. Ghasemi, G. Ni, A.M. Marconnet, J. Loomis, S. Yerci, N. Miljkovic, G. Chen, Solar steam generation by heat localization, Nat. Commun. 5 (2014) 7.
[10] P. Tao, G. Ni, C. Song, W. Shang, J. Wu, J. Zhu, G. Chen, T. Deng, Solar-driven interfacial evaporation, Nat. Energy 3 (2018) 1031–1041.
[11] Z. Wang, T. Horseman, A.P. Straub, N.Y. Yip, D. Li, M. Elimelech, S. Lin, Pathways and challenges for efficient solar-thermal desalination, Sci. Adv. 5 (2019), eaax0763.
[12] S. Cao, Q. Jiang, X. Wu, D. Ghim, H.G. Derami, P.-I. Chou, Y.-S. Jun, S. Singamaneni, Advances in solar evaporator materials for freshwater generation, J. Mater. Chem. 7 (2019) 24092–24123.
[13] J.U. Kim, S. Lee, S.J. Kang, T.-i. Kim, Materials and design of nanostructured broadband light absorbers for advanced light-to-heat conversion, Nanoscale 10 (2018) 21555–21574.
[14] H. Liu, Z. Huang, K. Liu, X. Hu, J. Zhou, Interfacial solar-to-heat conversion for desalination, Adv. Energy Mater. 9 (2019), 1900310.
[15] J. Zhou, Y. Gu, P. Liu, P. Wang, L. Miao, J. Liu, A. Wei, X. Mu, J. Li, J. Zhu, Development and evolution of the system structure for highly efficient solar steam generation from zero to three dimensions, Adv. Funct. Mater. 29 (2019), 1903255.
[16] L. Zhou, Y. Tan, J. Wang, W. Xu, Y. Yuan, W. Cai, S. Zhu, J. Zhu, 3D self-assembly of aluminium nanoparticles for plasmon-enhanced solar desalination, Nat. Photonics 10 (2016) 393–398.
[17] Z. Wang, Y. Liu, P. Tao, Q. Shen, N. Yi, F. Zhang, Q. Liu, C. Song, D. Zhang, W. Shang, T. Deng, Bio-inspired evaporation through plasmonic film of nanoparticles at the air-water interface, Small 10 (2014) 3234–3239.
[18] K. Bae, G. Kang, S.K. Cho, W. Park, K. Kim, W.J. Padilla, Flexible thin-film black gold membranes with ultrabroadband plasmonic nanofocusing for efficient solar vapour generation, Nat. Commun. 6 (2015) 10103.
[19] Z. Yin, H. Wang, M. Jian, Y. Li, K. Xia, M. Zhang, C. Wang, Q. Wang, M. Ma, Q.-s. Zheng, Y. Zhang, Extremely black vertically aligned carbon nanotube Arrays for solar steam generation, Acs Appl. Mater. Inter. 9 (2017) 28596–28603.
[20] M. Sun, C. Boo, W. Shi, J. Rolf, E. Shaulsky, W. Cheng, D.L. Plata, J. Qu, M. Elimelech, Engineering carbon nanotube forest superstructure for robust thermal desalination membranes, Adv. Funct. Mater. 29 (2019), 19013125.
[21] D. Weng, F. Xu, X. Li, Y. Li, J. Sun, Bioinspired photothermal conversion coatings with self-healing superhydrophobicity for efficient solar steam generation, J. Mater. Chem. 6 (2018) 24441–24451.
[22] H. Liang, Q. Liao, N. Chen, Y. Liang, G. Lv, P. Zhang, B. Lu, L. Qu, Thermal efficiency of solar steam generation approaching 100% through capillary water transport, Angew. Chem. Int. Ed. 58 (2019) 19041–19046.
[23] P. Zhang, J. Li, L. Lv, Y. Zhao, L. Qu, Vertically aligned graphene sheets membrane for highly efficient solar thermal generation of clean water, ACS Nano 11 (2017) 5087–5093.
[24] Z. Xie, Y. Duo, Z. Lin, T. Fan, C. Xing, L. Yu, R. Wang, M. Qiu, Y. Zhang, Y. Zhao, X. Yan, H. Zhang, The rise of 2D photothermal materials beyond graphene for clean water production, Adv. Sci. 7 (2020), 1902236.
[25] X. Hu, W. Xu, L. Zhou, Y. Tan, Y. Wang, S. Zhu, J. Zhu, Tailoring graphene oxide-based aerogels for efficient solar steam generation under one sun, Adv. Mater. 29 (2017), 1604031.
[26] Y. Guo, H. Lu, F. Zhao, X. Zhou, W. Shi, G. Yu, Biomass-derived hybrid hydrogel evaporators for cost-effective solar water purification, Adv. Mater. 32 (2020), 1907061.
[27] F. Zhao, X. Zhou, Y. Shi, X. Qian, M. Alexander, X. Zhao, S. Mendez, R. Yang, L. Qu, G. Yu, Highly efficient solar vapour generation via hierarchically nanostructured gels, Nat. Nanotechnol. 13 (2018) 489–495.
[28] Y. Guo, X. Zhou, F. Zhao, J. Bae, B. Rosenberger, G. Yu, Synergistic energy nanoconfinement and water activation in hydrogels for efficient solar water desalination, ACS Nano 13 (2019) 7913–7919.
[29] X. Zhou, F. Zhao, Y. Guo, B. Rosenberger, G. Yu, Architecting highly hydratable polymer networks to tune the water state for solar water purification, Sci. Adv. 5 (2019), eaaw5484.
[30] Y. Guo, F. Zhao, X. Zhou, Z. Chen, G. Yu, Tailoring nanoscale surface topography of hydrogel for efficient solar vapor generation, Nano Lett. 19 (2019) 2530–2536.
[31] X. Zhou, F. Zhao, Y. Guo, Y. Zhang, G. Yu, A hydrogel-based antifouling solar evaporator for highly efficient water desalination, Energy Environ. Sci. 11 (2018) 1985–1992.
[32] J. Li, X. Zhou, J. Zhang, C. Liu, F. Wang, Y. Zhao, H. Sun, Z. Zhu, W. Liang, A. Li, Migration crystallization device based on biomass photothermal materials for efficient salt-rejection solar steam generation, Acs Appl. Energ. Mater. 3 (2020) 3024–3032.
[33] R. Feng, Y. Qiao, C. Song, A perspective on bio-inspired interfacial systems for solar clean-water generation, Mrs Commun 9 (2019) 3–13.
[34] L. Yang, N. Li, C. Guo, J. He, S. Wang, L. Qiao, F. Li, L. Yu, M. Wang, X. Xu, Marine biomass-derived composite aerogels for efficient and durable solar-driven interfacial evaporation and desalination, Chem. Eng. J. (2020), 128051.
[35] N. Li, L. Qiao, J. He, S. Wang, L. Yu, P. Murto, X. Li, X. Xu, Solar-driven interfacial evaporation and self-powered water wave detection based on an all-cellulose monolithic design, Adv. Funct. Mater. 31 (2021), 2008681.
[36] N. Xu, X. Hu, W. Xu, X. Li, L. Zhou, S. Zhu, J. Zhu, Mushrooms as efficient solar steam-generation devices, Adv. Mater. 29 (2017), 1606762.
[37] C. Jia, Y. Li, Z. Yang, G. Chen, Y. Yao, F. Jiang, Y. Kuang, G. Pastel, H. Xie, B. Yang, S. Das, L. Hu, Rich mesostructures derived from natural woods for solar steam generation, Joule 1 (2017) 588–599.
[38] L. Yang, G. Chen, N. Zhang, Y. Xu, X. Xu, Sustainable biochar-based solar

absorbers for high-performance solar-driven steam generation and water purification, ACS Sustain. Chem. Eng. 7 (2019) 19311–19320.
[39] Y. Zhang, S.K. Ravi, J.V. Vaghasiya, S.C. Tan, A barbeque-analog route to carbonize moldy bread for efficient steam generation, iScience 3 (2018) 31–39.
[40] Y. Zhang, S.K. Ravi, S.C. Tan, Food-derived carbonaceous materials for solar desalination and thermo-electric power generation, Nanomater. Energy 65 (2019), 104006.
[41] X. Li, J. Li, J. Lu, N. Xu, C. Chen, X. Min, B. Zhu, H. Li, L. Zhou, S. Zhu, T. Zhang, J. Zhu, Enhancement of interfacial solar vapor generation by environmental energy, Joule 2 (2018) 1331–1338.
[42] K. Kim, S. Yu, S.-Y. Kang, S.-T. Ryu, J.-H. Jang, Three-dimensional solar steam generation device with additional non-photothermal evaporation, Desalination 469 (2019), 114091.
[43] H. Song, Y. Liu, Z. Liu, M.H. Singer, C. Li, A.R. Cheney, D. Ji, L. Zhou, N. Zhang, X. Zeng, Z. Bei, Z. Yu, S. Jiang, Q. Gan, Cold vapor generation beyond the input solar energy limit, Adv. Sci. 5 (2018), 1800222.
[44] C.A. Mullen, A.A. Boateng, N.M. Goldberg, I.M. Lima, D.A. Laird, K.B. Hicks, Bio-oil and bio-char production from corn cobs and stover by fast pyrolysis, Biomass Bioenergy 34 (2010) 67–74.
[45] C. Zhao, Q. Shao, Z. Ma, B. Li, X. Zhao, Physical and chemical characterizations of corn stalk resulting from hydrogen peroxide presoaking prior to ammonia fiber expansion pretreatment, Ind. Crop. Prod. 83 (2016) 86–93.
[46] B. Liu, T. Li, W. Wang, L.M.C. Sagis, Q. Yuan, X. Lei, M.A.C. Stuart, D. Li, C. Bao, J. Bai, Z. Yu, F. Ren, Y. Li, Corncob cellulose nanosphere as an eco-friendly detergent, Nat. Sustain. 3 (2020) 448–458.
[47] Y. Long, S. Huang, H. Yi, J. Chen, J. Wu, Q. Liao, H. Liang, H. Cui, S. Ruan, Y. Zeng, Carrot-inspired solar thermal evaporator, J. Mater. Chem. 7 (2019) 26911.
[48] J. Li, M. Du, G. Lv, L. Zhou, X. Li, L. Bertoluzzi, C. Liu, S. Zhu, J. Zhu, Interfacial solar steam generation enables fast-responsive, energy-efficient, and low-cost off-grid sterilization, Adv. Mater. 30 (2018), 1805159.
[49] J. Fang, J. Liu, J. Gu, Q. Liu, W. Zhang, H. Su, D. Zhang, Hierarchical porous carbonized Lotus seedpods for highly efficient solar steam generation, Chem. Mater. 30 (2018) 6217–6221.
[50] F. Gong, H. Li, W. Wang, J. Huang, D. Xia, J. Liao, M. Wu, D.V. Papavassiliou, Scalable, eco-friendly and ultrafast solar steam generators based on one-step melamine-derived carbon sponges toward water purification, Nanomater. Energy 58 (2019) 322–330.
[51] Y. Zhang, T. Xiong, L. Suresh, H. Qu, X. Zhang, Q. Zhang, J. Yang, S.C. Tan, Guaranteeing complete salt rejection by channeling saline water through fluidic photothermal structure toward synergistic zero energy clean water production and in situ energy generation, ACS Energy Lett 5 (11) (2020) 3397–3404.
[52] D. Van-Duong, H.-S. Choi, Carbon-based sunlight absorbers in solar-driven steam generation devices, Glob. Chall. 2 (2018), 170094.
[53] L. Zhu, M. Gao, C.K.N. Peh, X. Wang, G.W. Ho, Self-contained monolithic carbon sponges for solar-driven interfacial water evaporation distillation and electricity generation, Adv. Energy Mater. 8 (2018), 1702149.
[54] Y. Zhang, T. Xiong, D.K. Nandakumar, S.C. Tan, Structure architecting for salt-rejecting solar interfacial desalination to achieve high-performance evaporation with in situ energy generation, Adv. Sci. 7 (2020), 1903478.
[55] S. He, C. Chen, Y. Kuang, R. Mi, Y. Liu, Y. Pei, W. Kong, W. Gan, H. Xie, E. Hitz, C. Jia, X. Chen, A. Gong, J. Liao, J. Li, Z.J. Ren, B. Yang, S. Das, L. Hu, Nature-inspired salt resistant bimodal porous solar evaporator for efficient and stable water desalination, Energy Environ. Sci. 12 (2019) 1558–1567.
[56] G. Ni, S.H. Zandavi, S.M. Javid, S.V. Boriskina, T.A. Cooper, G. Chen, A salt-rejecting floating solar still for low-cost desalination, Energy Environ. Sci. 11 (2018) 1510–1519.
[57] Y. Kuang, C. Chen, S. He, E.M. Hitz, Y. Wang, W. Gan, R. Mi, L. Hu, A high-performance self-regenerating solar evaporator for continuous water desalination, Adv. Mater. 31 (2019), 1900498.
[58] Q. Huang, X. Liang, X. Zhang, C. Yan, J. Liang, H. Tang, Y. Liu, Efficient-heat-utilization 3D T-shaped porous sponge assists 2D photothermal films to achieve self-acting salt rejection and extra evaporation under high-concentration brine, Desalination 499 (2021), 114806.
[59] A.E. Burakov, E.V. Galunin, I.V. Burakova, A.E. Kucherova, S. Agarwal, A.G. Tkachev, V.K. Gupta, Adsorption of heavy metals on conventional and nanostructured materials for wastewater treatment purposes: a review, Ecotoxicol. Environ. Saf. 148 (2018) 702–712.
[60] L. Joseph, B.-M. Jun, J.R.V. Flora, C.M. Park, Y. Yoon, Removal of heavy metals from water sources in the developing world using low-cost materials: a review, Chemosphere 229 (2019) 142–159.
[61] M.K. Uddin, A review on the adsorption of heavy metals by clay minerals, with special focus on the past decade, Chem. Eng. J. 308 (2017) 438–462.
[62] Y. Wu, H. Pang, Y. Liu, X. Wang, S. Yu, D. Fu, J. Chen, X. Wang, Environmental remediation of heavy metal ions by novel-nanomaterials: a review, Environ. Pollut. 246 (2019) 608–620.